Cell rearrangement induced by filopodial tension accounts for the late phase of convergent extension in the sea urchin archenteron

Jeff Hardin[a],* and Michael Weliky[b]
[a]Department of Integrative Biology, University of Wisconsin, Madison, WI 53706; [b]Department of Brain and Cognitive Sciences, Center for Visual Science, University of Rochester, Rochester, NY 14627

ABSTRACT George Oster was a pioneer in using mechanical models to interrogate morphogenesis in animal embryos. Convergent extension is a particularly important morphogenetic process to which George Oster gave significant attention. Late elongation of the sea urchin archenteron is a classic example of convergent extension in a monolayered tube, which has been proposed to be driven by extrinsic axial tension due to the activity of secondary mesenchyme cells. Using a vertex-based mechanical model, we show that key features of archenteron elongation can be accounted for by passive cell rearrangement due to applied tension. The model mimics the cell elongation and the Poisson effect (necking) that occur in actual archenterons. We also show that, as predicted by the model, ablation of secondary mesenchyme cells late in archenteron elongation does not result in extensive elastic recoil. Moreover, blocking the addition of cells to the base of the archenteron late in archenteron elongation leads to excessive cell rearrangement consistent with tension-induced rearrangement of a smaller cohort of cells. Our mechanical simulation suggests that responsive rearrangement can account for key features of archenteron elongation and provides a useful starting point for designing future experiments to examine the mechanical properties of the archenteron.

INTRODUCTION

George Oster was a pioneer in using mechanical models to interrogate morphogenesis in animal embryos. He and his colleagues used Newtonian mechanics (Odell *et al.*, 1981; Jacobson *et al.*, 1986), and later, finite element continuum mechanical methods (Hardin and Cheng, 1986; Hardin and Keller, 1988), to test the biomechanical plausibility of proposed mechanisms of morphogenesis. For Oster, to borrow from D'Arcy Wentworth Thompson, the embryo was a "diagram of forces" at work within it.

The directed rearrangement of epithelial cells is a particularly important morphogenetic process during embryonic development

in metazoans to which Oster gave significant attention (Weliky and Oster, 1990; Weliky *et al.*, 1991). In many cases, cell rearrangement appears to be driven endogenously by the rearranging cells themselves. Examples include vertebrate neurulation (Jacobson and Gordon, 1976; Schoenwolf and Alvarez, 1989; Williams *et al.*, 2014), the ascidian notochordal primordium (Munro and Odell, 2002), *Drosophila* germ-band extension (Bertet *et al.*, 2004; Blankenship *et al.*, 2006; Simoes Sde *et al.*, 2010; Vanderleest *et al.*, 2018), and *Caenorhabditis elegans* dorsal epidermal intercalation (Williams-Masson *et al.*, 1998; Walck-Shannon *et al.*, 2015). The dominant force–producing systems vary among these examples; in some cases apical, asymmetric actomyosin contractility predominates; in other cases basolateral protrusive activity is more prominent (reviewed in Walck-Shannon and Hardin, 2014; Huebner and Wallingford, 2018).

As opposed to such "active" rearrangement, other examples of cell rearrangement appear to be "passive," that is, the forces driving cell neighbor exchange are dominated by external stress, such that cells rearrange to reduce the imposed stresses. Examples include cell rearrangement around embryonic wound sites (Honda *et al.*, 1982; reviewed in Jacinto *et al.*, 2001;

Hardin and Walston, 2004), the rearrangement of cells in amphibian ectodermal explants under externally applied loads (Beloussov et al., 2000), Drosophila wing disk morphogenesis (Umetsu et al., 2014), and contributions to germ-band extension in Drosophila (Butler et al., 2009).

Another system in which such passive rearrangement has been proposed to operate is the sea urchin archenteron, which has served as a classical paradigm for analyzing convergent extension in a monolayered epithelial tube (Ettensohn, 1985; Hardin and Cheng, 1986; Hardin, 1989; reviewed in Hardin, 1996; Wessel and Wikramanayake, 1999). The initial archenteron forms via primary invagination, which involves the bending of the vegetal plate inward to form a short, stout tube ~1/4 the diameter of the embryo with a blastoporal opening at its base. During this process cells involute over the blastopore lip, contributing to the developing archenteron (Ettensohn, 1985; Burke et al., 1991; Kimberly and Hardin, 1998). After a distinct pause in development (Gustafson and Kinnander, 1956), secondary mesenchyme cells (SMCs) become protrusively active, extending filopodia from the tip of the archenteron, marking the beginning of secondary invagination. During secondary invagination the archenteron narrows and elongates until it ultimately contacts the animal pole. Cells are added to the base of the archenteron during secondary invagination via additional involution (Logan and McClay, 1997; Martins et al., 1998; Piston et al., 1998; Ransick and Davidson, 1998).

Older descriptive studies revealed (Ettensohn, 1985; Hardin and Cheng, 1986; Hardin, 1989), and more recent high-resolution lineage tracing have confirmed (Martik and McClay, 2017) that arch-enteron cells undergo convergent extension during secondary invagination. The initial phase of secondary invagination is driven by active rearrangement. Ablation of SMCs does not prevent the initial elongation of the archenteron, nor does it result in noticeable retraction of the archenteron (Hardin, 1988), and the archenteron can partially elongate in embryos in which the gut rudiment is everted (Hardin and Cheng, 1986).

Studies using several species have suggested that filopodial tension plays a more prominent role late in gastrulation (Dan and Okazaki, 1956; Kinnander and Gustafson, 1960; Hardin, 1988). That SMCs can exert tension is indicated by the presence of "cones of attachment" where they make connections to the blastocoel roof (Gustafson and Kinnander, 1960; reviewed in Hardin, 1996). Completion of archenteron elongation appears to require traction by SMCs. Cells in the archenteron elongate at the 2/3 gastrula stage, consistent with this suggestion (Hardin, 1989), and ablation of all SMCs leads to cessation of elongation (Hardin, 1988). Moreover, the fully elongated archenteron is characterized by "necking" (the Poisson effect), that is, narrowing in the central region of the tube (Hardin and Cheng, 1986; Hardin, 1996).

One of us (M.W.) developed vertex-based mechanical models to investigate cell rearrangement in a variety of contexts during embryonic morphogenesis as a student in the Oster group (Weliky and Oster, 1990; Weliky et al., 1991). Another (J.H.) collaborated with one of George Oster's students to perform experiments alongside mechanical modeling of epithelial morphogenesis (Hardin and Cheng, 1986; Hardin and Keller, 1988). Here we combine modeling and experiment to show that passive rearrangement due to uniaxial stress is plausibly sufficient to account for the cell rearrangement and changes in cell shape that occur during the later stages of archenteron elongation. We also test predictions from the mechanical model regarding excessive rearrangement when the archenteron comprises fewer cells, and regarding stress relaxation in the archenteron due to passive rearrangement. Taken together, these results provide evidence that externally applied tension leads to cell rearrangement within the archenteron and should guide future experimental analyses of this classic morphogenetic system.
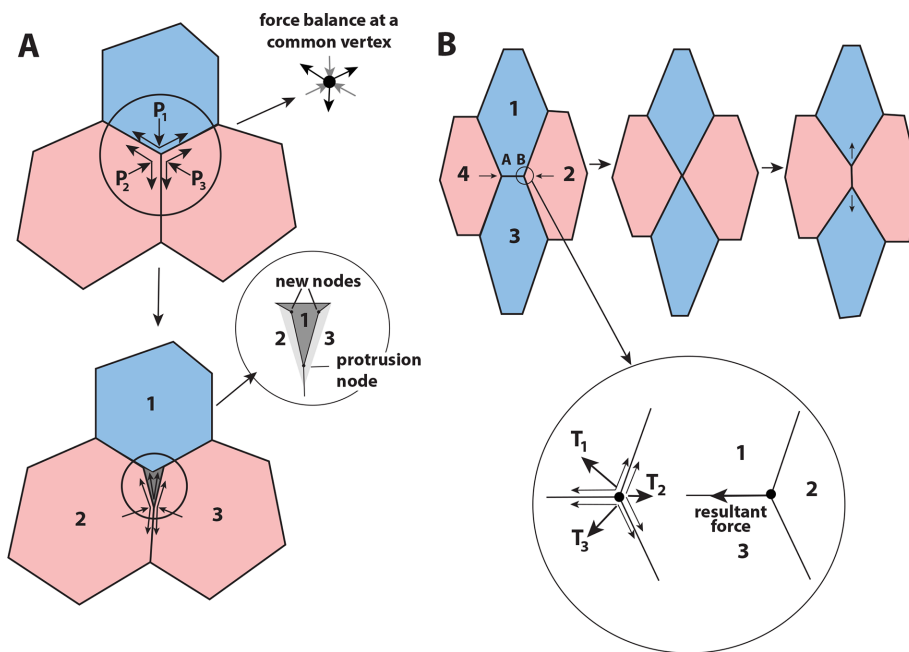

FIGURE 1: Vertex-based modeling of rearranging cells. For details of the model, see the text. (A) Adjacent cells share a common junctional vertex node. The node is in mechanical equilibrium when the pressure (P_i) and elastic forces (arrows parallel to membranes) from all cells are balanced. (B) Cell rearrangements can be constructed from the canonical situation illustrated in A. Four cells are shown. The pair of cells (cells 2 and 4), which are separated in the initial configuration, establish contact with one another. The remaining pair (cells 1 and 3), which are initially in contact with one another, separate. Cell rearrangement occurs when two nodes meet, and the junctions "change allegiance." Here, nodes A and B move toward one another. During junctional rearrangement, new nodes C and D are created, which subsequently separate. In the process edge AB has shortened and vanished, to be replaced by edge CD. The inset shows how the net force imbalance at node B causes the node to slide to the left. Adapted from Weliky and Oster (1990).

RESULTS AND DISCUSSION

Modeling the archenteron as a passively rearranging epithelium accounts for key features of late gastrulation

We used two-dimensional vertex-based modeling to explore whether passive rearrangement of archenteron cells induced by axial tension is sufficient to account for the basic features of late archenteron elongation. Brodland and colleagues have shown that such two-dimensional approximations capture salient features of the mechanics of epithelial monolayers as compared with full three-dimensional finite element approaches (Chen and Brodland, 2000; Hutson et al., 2009). The basic formalism of the model is shown in Figure 1; a monolayered
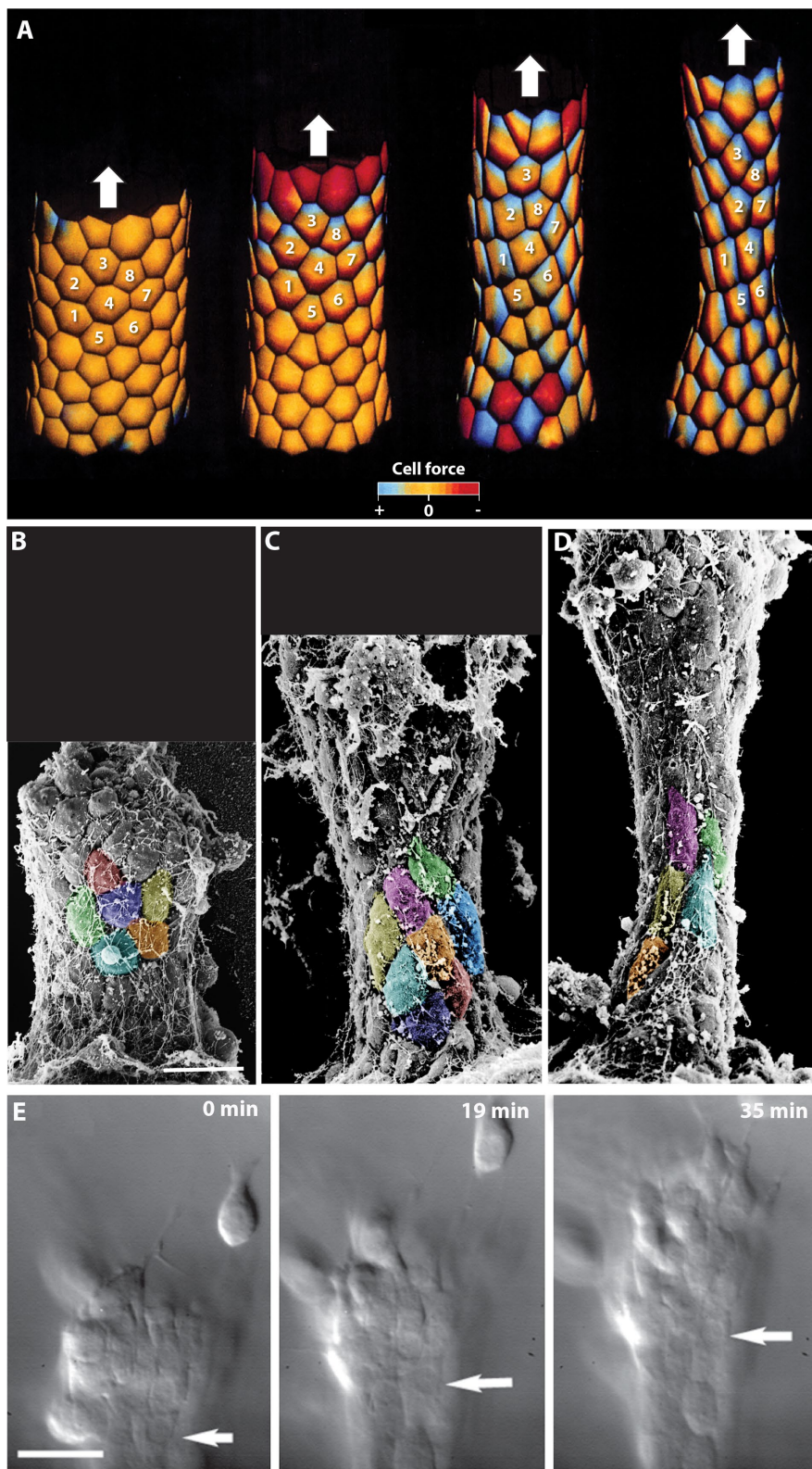
FIGURE 2: Modeling passive rearrangement via externally applied tension mimics key features of archenteron elongation in late *L. pictus* gastrulae. (A) The model archenteron. Warmer/redder colors indicate greater relative tension; cooler/bluer colors indicate less tension or compression. (B–E) Scanning electron micrographs of *L. pictus* archenterons at various stages of elongation. Groups of cells are colorized for clarity. (B, midgastrula; C, ⅔ gastrula; D, late gastrula). Scale bar = 10 μm. (E) Tension during archenteron elongation. Frames from a time-lapse movie of an *L. pictus* embryo at successive stages of archenteron elongation. The cell marked by the arrow undergoes elongation as gastrulation proceeds. Scale bar = 10 μm.

cylinder was modeled by enforcing an edge constraint on the model epithelium. Readers should consult *Materials and Methods* and Weliky and Oster (1990) for further details.

An example time-lapse series of a *Lytechinus pictus* gastrula during archenteron elongation is shown in Supplemental Video 1. Any successful model should account for several prominent features of late archenteron elongation: 1) cells in the archenteron elongate beginning at the 2/3 gastrula stage (Hardin, 1989); 2) cells continue to rearrange thereafter, but do so in a nonuniform manner, that is, the narrowest region of the archenteron has the fewest cells around its circumference; 3) cells in the narrowest region of the elongated archenteron are more elongated, a feature proposed to be due to the Poisson effect (Hardin, 1989); and 4) cell rearrangement should occur in the absence of multicellular rosettes like those seen in other systems (Blankenship *et al.*, 2006), that is, cell rearrangements in the archenteron are "T1" transitions, involving single neighbor exchanges as opposed to formation of transient foci, which then resolve (Fletcher *et al.*, 2014; Alt *et al.*, 2017).

We modeled the archenteron as a cylinder of cells that is pulled upward at the cylinder apex while the base of the tube is held stationary (Figure 2A; Supplemental Video 2). Contiguous cells (a group of eight such cells is numbered in Figure 2A) change position as elongation progresses. The result is elongation and narrowing of the cylinder. Cell rearrangements occur throughout the cylinder, such that the number of cells around the circumference decreases, while concomitantly the number of cells along the animal–vegetal (i.e., longitudinal) axis increases (A = 16 cells; B = 15 cells; C = 13 cells; D = 11 cells). A prominent feature of the simulation is the necking of the tube (Poisson effect) and the axial elongation of cells in this narrowed region in frames C and D. Moreover, as the coloring in Figure 2A and Supplemental Video 2 indicates, axial stress increases transiently (as indicated by warm colors) but dissipates substantially as cells continue to rearrange. Significantly, the simulation captures the pronounced necking behavior that occurs during secondary invagination, as exemplified by the scanning electron micrographs in Figure 2, B–D. Finally, in occasional embryos it is possible to resolve cell shapes in four-dimensional time-lapse sequences. Such sequences clearly show that cells in the archenteron
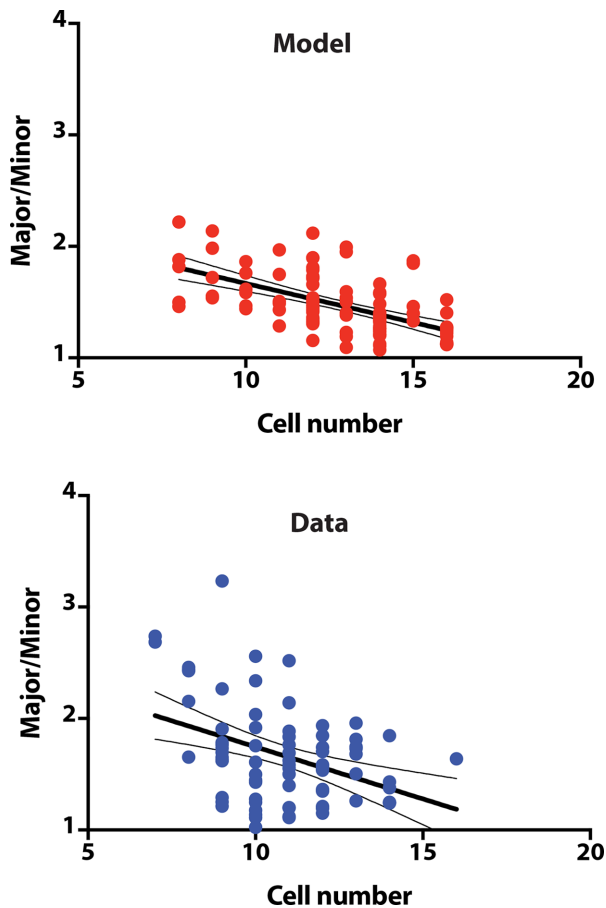
FIGURE 3: Correlation of cell elongation with extent of cell rearrangement in model and actual archenterons. The length/width ratios of cells in the model archenteron (top) and in actual archenterons processed for scanning electron microscopy were measured and plotted as a function of the number of cells around the circumference. Straight lines represent linear regression; curved lines indicate 95% confidence limits on the mean for each regression.

undergo stretching (Figure 2E) in a manner very similar to the cells in the model.

Next, we quantitatively compared the simulated archenteron to actual archenterons in terms of cell shape. In *L. pictus*, there is an increase in axial cell height beginning at the ¾ gastrula stage (Hardin, 1989). The simulation captures this increase: as circumferential cell number declines, there is a clear correlation with cell elongation in the simulation (slope = −0.07 ± 0.01, mean ± SEM, $n = 101$ cells; $r^2 = 0.33$; significant correlation, $p < 0.0001$) that compares favorably with measurements made on actual archenterons from specimens prepared for scanning electron microscopy (slope = −0.093 ± 0.03, mean ± SEM, $n = 78$ cells; $r^2 = 0.15$; significant correlation, $p = 0.0004$; Figure 3). In summary, the mechanical model reproduces key features of actual archenterons: 1) transient elongation of most cells in the cylinder; 2) additional cell rearrangement that is nonuniform along the animal–vegetal axis, and 3) elongation of cells in the narrowest region of the archenteron.

Perturbing attachment to the apical extracellular matrix blocks addition of cells to the base of the archenteron

Labeling experiments in both *Lytechinus variegatus* (Logan and McClay, 1997; Martins *et al.*, 1998; Piston *et al.*, 1998) and *Strongylocentrotus purpuratus* (Ransick and Davidson, 1998) em-

bryos indicate that late in gastrulation veg_1-derived cells contribute to the mid- and hindgut of the embryo via involution. The circumference of the blastopore decreases during late gastrulation in *L. pictus* as well, as cells rearrange at the base of the archenteron during the involution process (Hardin, 1989), a process we confirmed via two-photon imaging of living embryos (Supplemental Figure S1). Previous cell counts in *L. pictus* showed that the archenteron of the later gastrula comprises ~115–120 cells (Hardin, 1989). Cell counts in embryos that have completed gastrulation are much higher (~170; see below), consistent with the increase seen in *L. variegatus* embryos, in which late involution is known to occur (Logan and McClay, 1997; Martins *et al.*, 1998).

We sought to block the late addition of cells to the *L. pictus* archenteron by treating embryos with the monoclonal antibody mAb183, which recognizes the cell binding domain of the hyaline layer protein hyalin and perturbs cellular attachment to the hyaline layer (Adelson and Humphreys, 1988; Coffman and McClay, 1990). We found that treatment of *L. pictus* embryos with mAb183 during primary invagination had a striking effect on the subsequent morphology of the blastopore and development of the archenteron. Counts of the total number of cells in the archenteron in mAb183-treated late gastrulae indicated that involution is grossly perturbed in antibody-treated embryos; the average number of cells in the archenteron was 170 ± 10 (mean ± SEM) cells ($n = 3$) compared with 90 ± 9 cells ($n = 5$; significantly different, $p = 0.025$, Mann-Whitney U test). The overt phenotypes of mAb183-treated embryos indicated that their primary defect is failure of involution. In all classes of embryos examined, the vegetal epithelium underwent distension consistent with prevention of the second, late phase of involution (see Figure 4).

To examine the effects of perturbing cell attachment to the hyaline layer on blastopore cell shape and behavior at the midgastrula stage, we labeled cells with fluorescent membrane dyes (Supplemental Table 1). FM4-64 labeling of blastoporal cells in mAb183-treated embryos (length width ratio = 1.96 ± 0.10, $n = 199$ cells; mean ± SEM) indicated that blastoporal cells are significantly more circumferentially elongated than in normal midgastrula embryos (1.40 ± 0.07, $n = 224$ cells; $p = 0.0001$). This may reflect the inability of the blastoporal epithelium to accommodate hoop stress associated with blastopore closure.

We next used two-photon microscopy to compare the motility of cells in normal and mAb183-treated embryos sparsely labeled with the lipophilic dye, $DiIC_{16}$. Cells at the blastopore displayed dynamic protrusions during blastopore closure as they changed their contacts with one another (Supplemental Figure S1). There was a significant difference between the length of filopodia of blastopore cells in mAb183-treated midgastrula embryos (2.83 ± 0.13 μm; $n = 199$ protrusions) versus normal embryos (1.88 ± 0.08 μm; $n = 224$; $p = 0.001$), but other characteristics were nearly identical (Supplemental Figure S1; Supplemental Table 1). Thus, polarized motility is largely normal at the blastopore in mAb183-treated embryos, but the ability of cells to involute over the blastopore lip late in gastrulation is blocked.

Apical extracellular matrices are known to play significant roles in several embryonic epithelia (Jazwinska *et al.*, 2003; Mancuso *et al.*, 2012). There are several possible ways by which attachment to the hyaline layer could aid late involution. One possibility is that the hyaline layer serves as a mechanically resistive extracellular matrix, forcing cells into the interior as they rearrange at the blastopore. A similar role for a mechanically constraining extracellular layer has been suggested in the case of the *Xenopus* gastrula, where it has been anecdotally observed that the frequency of exogastrulation
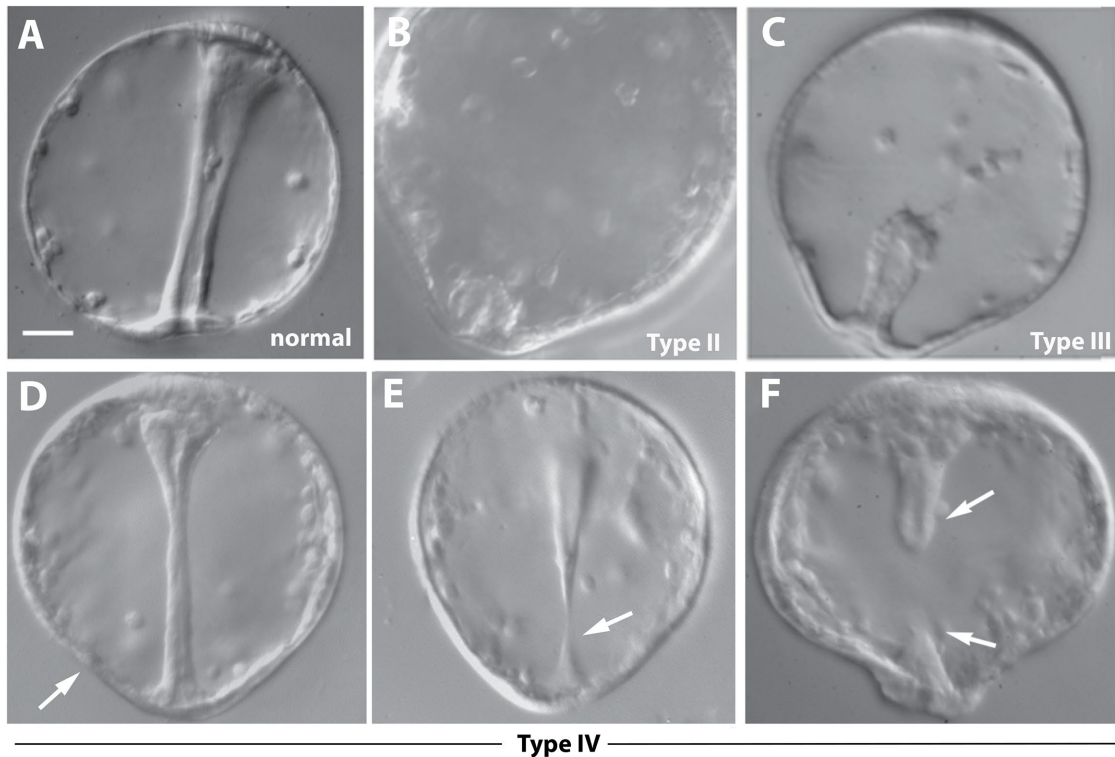
FIGURE 4: mAb183 treatment leads to excessive rearrangement in the archenteron. (A) mAb183 was added to the *L. pictus* embryo cultures when they had developed to the midprimary invagination stage. Four different types of embryos developed following treatment with mAb183. The first type completely loses its invagination and develops a protruding vegetal pole epithelium (unpublished data). (B) The second type retains a small invagination at the vegetal pole; however, it does not elongate and the vegetal epithelium protrudes. (C) The third type of embryo retains its archenteron, which appears to undergo a limited amount of elongation; however, it remains short and the vegetal epithelium is distended. (D) A control late gastrula embryo of the same temporal age as the mAb183-treated embryos in B and C and E and F. The vegetal epithelium does not protrude and the archenteron has a normal lumen and length. (D, E) Two mAb183-treated late gastrulae with abnormally thin archenterons compared with archenteron width of the control in D. In E the midpoint of the archenteron is only one cell wide (arrow). Both embryos in E and F have protruding vegetal epithelia (E, arrow). (F) In some type IV embryos the archenteron rips in two and the two fragments seal their open ends (arrows). Scale bar = 10 μm.

increases following surgical removal of the vitelline envelope (Hardin and Keller, 1988).

Forcing the archenteron to elongate with fewer cells leads to excessive rearrangement

We next exploited mAb183-treated embryos as a tool to assess our mechanical model. A key prediction of the model is that tension-induced rearrangement should be more pronounced in mAb183 embryos, because a cylinder with fewer total cells must span the same distance along the animal–vegetal axis. We obtained phenotypes consistent with this prediction. When mAb183 was added to cultures during midprimary invagination, four different phenotypes were obtained, based on the types of defects and the stage at which the phenotype becomes apparent (Figure 4). All of the embryos had initiated archenteron formation, as primary invagination was well underway at the time of mAb183 application. In the first three types of embryos, the protruding epithelium became apparent while controls were still completing primary invagination. In 20% of embryos examined ($n = 55$), there was no archenteron, but instead a completely everted vegetal epithelium (type I embryos; unpublished data). Twenty percent of treated embryos had a very short archenteron that does not elongate and a protruding vegetal epithelium (type II; Figure 4B). Twenty-two percent of treated embryos had a

short archenteron that appeared to undergo some elongation (type III; Figure 4C). In 27% of treated embryos, the vegetal epithelium appeared normal through late gastrulation (type IV). The archenteron in these embryos contacted the animal pole but appeared thinner than normal. As the controls approached the early prism stage, the vegetal epithelium began to protrude in these embryos, forming a "collar" of tissue at the blastopore (Figure 4, D and E). As these embryos continued to develop, their archenterons became highly elongated and narrow compared with controls. Remarkably, in some type IV embryos the archenteron was only one cell wide in the middle and did not have a continuous lumen (Figure 4E); in other cases, the archenteron ripped in two, and the torn edges underwent wound healing to seal the open ends (Figure 4F). These effects are consistent with excessive passive rearrangement among a smaller cohort of endodermal cells to which the same uniaxial stretch was applied by secondary mesenchyme at the tip of the archenteron.

Laser ablation of SMCs late in gastrulation does not lead to retraction of the archenteron

We performed an additional simple experiment. The model predicts that passive rearrangement should dissipate stress within the archenteron via what amounts to a plastic deformation of the archenteron. Thus, there should be little viscoelastic recoil of the
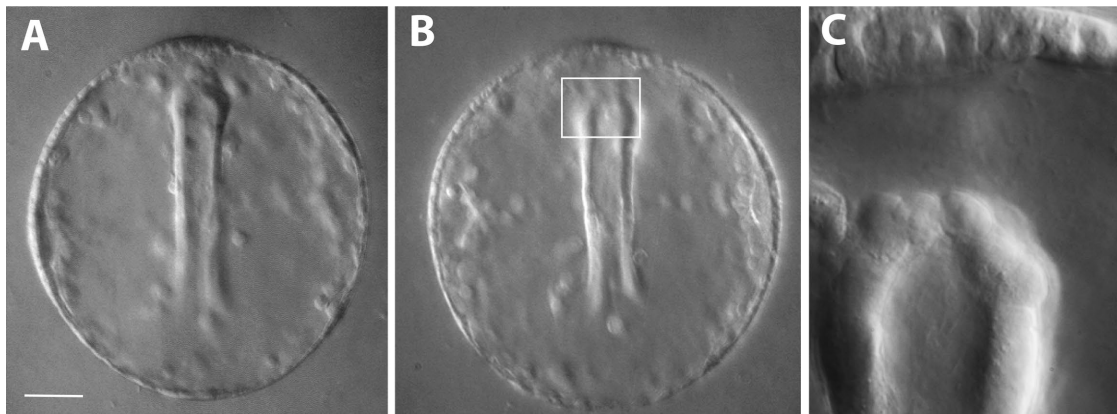
FIGURE 5: The archenteron does not retract following ablation of SMCs. (A) A late *L. pictus* gastrula near the end of gastrulation, but before contact of the tip of the archenteron with the animal pole. (B) The same embryo following ablation of the tip of the archenteron. Little retraction of the archenteron occurs. (C) Inset of the boxed region in B. Scale bar = 10 μm.

archenteron when SMCs are ablated late in gastrulation, after such plastic deformation. We tested this prediction by performing laser ablation of SMCs near the end of gastrulation, after most rearrangement has occurred. We found that there was very little retraction of the archenteron when SMCs at the tip of the archenteron were ablated (Figure 5, A and B; retraction distance ≤5 μm; *n* = 3 embryos), consistent with the mechanical model's prediction.

Passive rearrangement is a sufficient morphogenetic mechanism to account for late archenteron elongation

How cell rearrangement occurs in epithelia subjected to external stress is poorly understood, especially in the context of intact embryonic tissues. Our mechanical simulation suggests that responsive rearrangement can account for key features of a paradigmatic example of such a morphogenetic event—sea urchin archenteron extension. Recent work, much of it in *Drosophila* embryos, has implicated pulsatile actomyosin-mediated contractility during epithelial morphogenesis (Martin *et al.*, 2009; Rauzi *et al.*, 2010; Levayer and Lecuit, 2013; Simoes Sde *et al.*, 2014; Shindo *et al.*, 2018; Vanderleest *et al.*, 2018) reviewed in Huebner and Wallingford (2018). One frequently proposed role for such pulsatile behavior is that it allows for dynamic repositioning of cell–cell contacts. A recent mechanical model has incorporated such pulsatile actomyosin dynamics in the case of deep cells in the *Xenopus* embryo (Shindo *et al.*, 2018). It will be interesting to examine epithelia that undergo passive rearrangement like the sea urchin archenteron to determine what role such pulsatility plays in situations where the predominant mechanical influence is extrinsic versus intrinsic.

Several additional questions remain unanswered by our simulations. First, we have not modeled early phases of archenteron morphogenesis. Two-dimensional vertex models may not be able capture the complex apicobasal differences in cell shape during primary invagination. A true three-dimensional modeling scheme may be necessary in this case. Second, we did not model the early phase of archenteron elongation, when active rearrangement, as opposed to passive response to axial tension, predominates. Such modeling may be possible using a two-dimensional vertex-based model, but will require a better understanding of the subcellular forces that operate during the initial phase of secondary invagination. Finally, a detailed, quantitative understanding of the combined contributions of cell–cell adhesion and interactions with the basal and apical extracellular matrices to the mechanical properties of the

archenteron awaits further investigation. Nevertheless, our mechanical modeling provides a useful starting point for designing such insightful future experiments to explore these aspects of cell rearrangement. As George Oster was so fond of saying, experimental validation of such models is the "ultimate compliment" to the theoretical biologist.

MATERIALS AND METHODS
Modeling procedures
Construction of polygonal nodes. The model epithelium consists of a sheet of two-dimensional polygons whose sides are shared by neighboring cells. Each epithelial cell is modeled as a two-dimensional polygon (i.e., as a collection of nodes connected by line segments) with a variable number of nodes that typically range from four to seven. The polygonal nodes are placed at each apex, which forms the junction between three cells. Each polygon has a variable number of sides and nodes can slide so that the length of a side is also variable.

Tessellation of a plane into Voronoi polygons. The starting configuration of cell shapes and sizes was determined by assigning nuclear positions and constructing a Voronoi polygon about each point. Details regarding initial mesh construction are described in Weliky and Oster (1990).

Modeling a cell. Cells in the mechanical model originally developed by Weliky and Oster (1990) were capable of both contractile and protrusive behavior. Elastic tensions are assigned to each polygonal segment, and an internal pressure to each polygonal area. The central features of the model are illustrated in Figure 1. We represent each cell by a two-dimensional polygon (i.e., as a collection of nodes connected by line segments) with a variable number of sides. At each node we calculate the balance of elastic tension and pressure forces. The pressure vector, P, is directed outward from the cell boundary at each node. Two elastic tension vectors are applied to each node and are directed along the polygonal cell edges (Figure 1A). The magnitude of these vectors represents the local elastic tension at each cell node. Specifically, the elastic tension forces at cell node, *n*, are represented by a pair of two-dimensional vectors, $T_{(n,n-1)}$ and $T_{(n,n+1)}$, applied to the node (Figure 1B). The pressure at each node is represented by the two-dimensional pressure vector *P* directed normal to the polygonal surface at each

node. The two-dimensional unit surface normal vector P describes the direction of the nodal pressure, and its magnitude varies inversely with the area of the cell.

The net force acting at a cell node, n, is the vector sum of the nodal tensions and pressure: $F_n = P + T_{(n,n-1)} + T_{(n,n+1)}$. The total force acting at an epithelial node is the sum of all net forces from all cells sharing this node plus the external forces:

$$\sum_{(n=1)}^{N} F_n + F_{ext}$$

where N is the number of cells sharing the common junctional node.

The net force at each cell node is thus the sum of the pressure and elastic forces, and the shape of the cell boundary reflects the relative balance of elastic and pressure forces at each node. If the elastic forces at all nodes are equal (i.e., the cell is contracting equally all around its periphery), the cell will relax to a regular polyhedral form. For a polygonal cell with a large number of faces, the cell approaches a circular shape. The cell shape remains stable so long as all nodal tensions and pressures are in mechanical equilibrium.

Modeling a tissue capable of T1 rearrangements. To model and simulate a tissue, a large number of polygonal cells are coupled together. This is accomplished by allowing adjacent cells to share common boundary nodes. Junctional nodes can slide, and nodes may appear or disappear as necessary, so that the number of polygonal sides is variable. Cell rearrangement occurs when two nodes are less than a minimum threshold distance apart (the threshold distance is made very small relative to the size of the cells). During such events, one pair of cells previously in contact separate while the second pair of cells, which were previously separated, establish contact (Figure 1B). External forces may be applied to the boundaries of the tissue. The total force acting at a node in this case is the sum of all net forces from all cells sharing this node plus any external forces.

Passive cell rearrangement. Application of the model to actively rearranging tissues can be found in Weliky *et al.* (1991). Here we modeled a two-dimensional cylinder undergoing purely passive rearrangement. As an epithelial sheet is stretched by external forces applied to the epithelial margin, cells will "passively" elongate in the direction of the applied force (Figure 1B). Cells 1, 2, and 3 in Figure 1B share the circled junctional vertex node. Elongation of cells 1 and 3 increases their surface curvature at this node, while elongation of cell 2 decreases its curvature at this shared node. The net force at the node is represented by the vector resultant pointed in the direction of cells 1 and 3. Cell rearrangement occurs in order to restore each cell shape to a more isodiametric polygonal form.

Numerical solution of the equations of motion and rendering. The equations of motion describing the model epithelium are a set of coupled differential equations in which the number of equations is equal to the number of nodes in the simulation, which can be many hundreds. Because the equations are nonlinear, an analytical solution to this system is not possible, requiring the application of numerical methods. The numerical solution involves the conversion of the differential equations to finite difference equations. The mechanical force balance equations are iteratively solved using numerical techniques. The simulation proceeds by repeatedly solving the equations of motion for each cell node during each iteration. During each iteration a node moves a distance proportional to the total force applied to that node. The arrangement resulting from the node displacements in one iteration becomes the starting point for the next iteration. Nodes and vertices were rendered as described previously (Weliky and Oster, 1990).

Embryo culture and time-lapse microscopy
Adult *L. pictus* sea urchins were obtained from Marinus (Long Beach, CA) and intracoelomic injection of 0.5 M KCl was used to induce gamete shedding. The eggs were filtered through cheesecloth to remove the jelly coats, fertilized with dilute sperm, and the resulting embryos were reared in stirring cultures in artificial seawater (ASW) at 14–19°C. For Nomarski time-lapse microscopy, embryos were mounted on poly-L-lysine–coated coverslips, ringed with mineral oil, and supported on microscope slides using silicone vacuum grease as previously described (Hardin, 1989). Images were acquired on a Nikon Optiphot II microscope using an oil-immersion 1.4 NA 60× Planapo lens and a Newvicon video camera, and digitized using a custom version of National Institutes of Health (NIH) Image as described (Kimberly and Hardin, 1998) or using a FireWire QiCam camera (QImaging) and MicroManager software (Edelstein *et al.*, 2014). Movies were processed using 32-bit ImageJ (Schneider *et al.*, 2012) and QuickTime for Java as described in detail elsewhere (Hardin, 2011) or exported as AVIs via Fiji (Schindelin *et al.*, 2012) and converted to MP4 movies using MPEG Streamclip (www.squared5.com).

mAb183 treatment
Midprimary invagination stage embryos were transferred to ASW containing 30 µg/ml of the monoclonal antibody 183 (mAb183) purified from ascites fluid (kindly provided by T. Humphreys [Kewalo Marine Institute, University of Hawaii–Manoa]; Adelson and Humphreys, 1988). mAb183 binds the protein hyalin and blocks normal gastrulation at this concentration (Adelson and Humphreys, 1988). The mAb183-treated embryos were cultured in wells of a microtiter plate at 15°C until untreated, control embryos cultured in the same microtiter plate had reached the desired stage for imaging.

Fluorescence labeling of embryos for archenteron and blastopore cell counts
For counting the number of cells in the archenteron of mAb183-treated or normal embryos, embryos at the early prism stage were fixed for 10 min at room temperature in a freshly made 2% paraformaldehyde solution in ASW. Embryos were washed three times in phosphate-buffered saline (PBS) and then incubated in PBS + 1 µg/ml 4′,6-diamidino-2-phenylindole (DAPI) solution for 10 min. The embryos were washed three times in PBS and mounted between a coverslip and microscope slide with four dots of silicon grease at each corner as a support.

For counting the number of blastopore cells in mAb183-treated and normal late prism stage embryos, the embryos were incubated in ASW + 1 µg/ml of the lipophilic membrane dye FM4-64 (Molecular Probes, Eugene, OR) for 1 min. After two washes in ASW, the embryos were mounted as described for two-photon imaging and imaged using epifluorescence microscopy on a Nikon Optiphot II microscope using a 60× Planapo oil-immersion objective (NA = 1.4). Images were acquired using a Hamamatsu Orca I cooled CCD camera and QED Imaging software (QED Imaging, Pittsburgh, PA). The number of nuclei in the archenteron and the number of cells at the blastopore lip in mAb183-treated and normal late prism stage embryos was counted using a modified version of NIH Image.

Measurement of cell shape and statistical analysis
Processing of embryos for scanning electron microscopy was performed as described in Hardin and Cheng (1986) and Hardin (1989). Cells boundaries were traced from scanning electron micrographs

using Fiji, exported to Microsoft Excel, and then imported into GraphPad Prism. Linear regression, correlation analysis, and graphing were performed in Prism. Colorized SEMs were produced using Adobe Photoshop.

DiIC$_{16}$ labeling of embryos and two-photon microscopy

mAb183-treated or normal embryos at the stage of interest were incubated in ASW + 5 µg/ml of the lipophilic membrane dye DiIC$_{16}$ (Molecular Probes, Eugene, OR) for 1–5 min. The dye sparsely labels surface epithelial cells at random. After two washes in ASW, the embryos were mounted as described below and imaged using two-photon microscopy. Four dots of silicon vacuum grease (Dow Corning) were placed at the corners of coverslips precoated with 0.1% poly-l-lysine (Sigma). Approximately 50 µl of ASW containing normal midgastrulae, late gastrulae, or the equivalent stages of mAb183-treated embryos were mouth-pipetted onto the coverslip. While observing the embryos under a dissecting microscope (Wild, Heerbrug, Switzerland), they were oriented so that their vegetal plates were parallel to the coverslip using a glass microneedle made by hand-pulling a 5 ml micropipette (Fisher) in a Bunsen burner flame. A ring of mineral oil (Sigma) was pipetted around the ASW and a slide was placed over the coverslip and compressed slightly. More mineral oil was pipetted under the coverslip to minimize evaporation.

The two-photon system consisted of a Nikon Diaphot inverted microscope equipped with an Nd:YLF laser and BioRad MRC-600 apparatus configured as described by Wokosin et al. (1996). No pinhole was inserted in the optical path. The signal generated by two-photon excitation was descanned into the MRC-600 scanhead and detected by internal photomultipliers. A 60× oil-immersion objective (NA = 1.4; Nikon) was used to collect images. Time-lapse recordings were performed using two-photon microscopy; individual frames were acquired at 30-s intervals.

Quantification of cell and filopodial characteristics

The center of the blastopore in each embryo served as a fixed point from which to examine the relative orientation of cells and their filopodia (Supplemental Figure S1). We determined the Feret length/width ratio of the cells by drawing the radius connecting the center of the blastopore with the center of the cell, and then measuring the longest axis of the cell perpendicular to this radius (Supplemental Figure S1A).

In addition, three different filopodium measurements were made. First, the length of the filopodium was measured from its base to its tip (F; Supplemental Figure S1A). Second, the angular orientation of a filopodium, relative to a line normal to a radius drawn from the center of the blastopore to the center of the cell, provided a measure of the filopodium's orientation relative to the blastopore circumference. Third, the position of a filopodium along the same axis reflected its degree of polarity (λ; Supplemental Figure S1A). A ratio of filopodial position to total Feret length was determined for each filopodium measured ("polarization"; Supplemental Figure S1A), using the center of the cell along the circumblastoporal axis as the origin. Thus, a large filopodium position to Feret length indicated a more polarized filopodium (i.e., the filopodium was extended from near one end of the cell rather than the middle). In the raw data calculations the maximum possible Feret ratio equaled 0.5. For ease of comparison, the data were then multiplied by 2 so that the maximum adjusted polarization was 1.0. Finally, the persistence of the filopodia was determined by noting the number of time frames in which they remained extended.

Statistical analysis of the data was completed using Statview II v. 2.0 (Abacus Concepts, Berkeley, CA). Because the data were not normally distributed, comparisons between normal midgastrulae versus normal late gastrulae, normal midgastrulae versus mAb183-treated midgastrulae, and normal late gastrulae versus mAb183-treated late gastrulae cell and filopodial measurements were made using the Mann-Whitney U test at a 95% confidence interval. Angular statistical analysis was completed using a computer running Mac OS 9 and the program CircleStat (developed by J.H. and available upon request).

REFERENCES

Adelson DL, Humphreys T (1988). Sea urchin morphogenesis and cell-hyalin adhesion are perturbed by a monoclonal antibody specific for hyalin. Development 104, 391–402.

Alt S, Ganguly P, Salbreux G (2017). Vertex models: from cell mechanics to tissue morphogenesis. Philos Trans R Soc Lond B Biol Sci 372, 20150520.

Beloussov LV, Louchinskaia NN, Stein AA (2000). Tension-dependent collective cell movements in the early gastrula ectoderm of Xenopus laevis embryos. Dev Genes Evol 210, 92–104.

Bertet C, Sulak L, Lecuit T (2004). Myosin-dependent junction remodelling controls planar cell intercalation and axis elongation. Nature 429, 667–671.

Blankenship JT, Backovic ST, Sanny JS, Weitz O, Zallen JA (2006). Multicellular rosette formation links planar cell polarity to tissue morphogenesis. Dev Cell 11, 459–470.

Burke RD, Myers RL, Sexton TL, Jackson C (1991). Cell movements during the initial phase of gastrulation in the sea urchin embryo. Dev Biol 146, 542–557.

Butler LC, Blanchard GB, Kabla AJ, Lawrence NJ, Welchman DP, Mahadevan L, Adams RJ, Sanson B (2009). Cell shape changes indicate a role for extrinsic tensile forces in Drosophila germ-band extension. Nat Cell Biol 11, 859–864.

Chen HH, Brodland GW (2000). Cell-level finite element studies of viscous cells in planar aggregates. J Biomech Eng 122, 394–401.

Coffman JA, McClay DR (1990). A hyaline layer protein that becomes localized to the oral ectoderm and foregut of sea urchin embryos. Dev Biol 140, 93–104.

Dan K, Okazaki K (1956). Cyto-embryological studies of sea urchins. III. Role of the secondary mesenchyme cells in the formation of the primitive gut in sea urchin larvae. Biol Bulletin 110, 29–42.

Edelstein AD, Tsuchida MA, Amodaj N, Pinkard H, Vale RD, Stuurman N (2014). Advanced methods of microscope control using µManager software. J Biol Methods 1, e10.

Ettensohn CA (1985). Gastrulation in the sea urchin embryo is accompanied by the rearrangement of invaginating epithelial cells. Dev Biol 112, 383–390.

Fletcher AG, Osterfield M, Baker RE, Shvartsman SY (2014). Vertex models of epithelial morphogenesis. Biophys J 106, 2291–2304.

Gustafson T, Kinnander H (1956). Microaquaria for time-lapse cinematographic studies of morphogenesis in swimming larvae and observations on sea urchin gastrulation. Exp Cell Res 11, 36–51.

Gustafson T, Kinnander H (1960). Cellular mechanisms in morphogenesis of the sea urchin gastrula. The oral contact. Exp Cell Res 21, 361–373.

Hardin J (1988). The role of secondary mesenchyme cells during sea urchin gastrulation studied by laser ablation. Development 103, 317–324.

Hardin J (1989). Local shifts in position and polarized motility drive cell rearrangement during sea urchin gastrulation. Dev Biol 136, 430–445.

Hardin J (1996). The cellular basis of sea urchin gastrulation. Curr Top Dev Biol 33, 159–262.

Hardin J (2011). Imaging embryonic morphogenesis in *C. elegans*. Methods Cell Biol 106, 377–412.

Hardin JD, Cheng LY (1986). The mechanisms and mechanics of archenteron elongation during sea urchin gastrulation. Dev Biol 115, 490–501.

Hardin J, Keller R (1988). The behaviour and function of bottle cells during gastrulation of *Xenopus laevis*. Development 103, 211–230.

Hardin J, Walston T (2004). Models of morphogenesis: the mechanisms and mechanics of cell rearrangement. Curr Opin Genet Dev 14, 399–406.

Honda H, Ogita Y, Higuchi S, Kani K (1982). Cell movements in a living mammalian tissue: long-term observation of individual cells in wounded corneal endothelia of cats. J Morphol 174, 25–39.

Huebner RJ, Wallingford JB (2018). Coming to consensus: a unifying model emerges for convergent extension. Dev Cell 46, 389–396.

Hutson MS, Veldhuis J, Ma X, Lynch HE, Cranston PG, Brodland GW (2009). Combining laser microsurgery and finite element modeling to assess cell-level epithelial mechanics. Biophys J 97, 3075–3085.

Jacinto A, Martinez-Arias A, Martin P (2001). Mechanisms of epithelial fusion and repair. Nat Cell Biol 3, E117–E123.

Jacobson AG, Gordon R (1976). Changes in the shape of the developing vertebrate nervous system analyzed experimentally, mathematically and by computer simulation. J Exp Zool 197, 191–246.

Jacobson AG, Oster GF, Odell GM, Cheng LY (1986). Neurulation and the cortical tractor model for epithelial folding. J Embryol Exp Morphol 96, 19–49.

Jazwinska A, Ribeiro C, Affolter M (2003). Epithelial tube morphogenesis during *Drosophila* tracheal development requires Piopio, a luminal ZP protein. Nat Cell Biol 5, 895–901.

Kimberly EL, Hardin J (1998). Bottle cells are required for the initiation of primary invagination in the sea urchin embryo. Dev Biol 204, 235–250.

Kinnander H, Gustafson T (1960). Further studies on the cellular basis of gastrulation in the sea urchin larva. Exp Cell Res 19, 278–290.

Levayer R, Lecuit T (2013). Oscillation and polarity of E-cadherin asymmetries control actomyosin flow patterns during morphogenesis. Dev Cell 26, 162–175.

Logan CY, McClay DR (1997). The allocation of early blastomeres to the ectoderm and endoderm is variable in the sea urchin embryo. Development 124, 2213–2223.

Mancuso VP, Parry JM, Storer L, Poggioli C, Nguyen KC, Hall DH, Sundaram MV (2012). Extracellular leucine-rich repeat proteins are required to organize the apical extracellular matrix and maintain epithelial junction integrity in *C. elegans*. Development 139, 979–990.

Martik ML, McClay DR (2017). New insights from a high-resolution look at gastrulation in the sea urchin, *Lytechinus variegatus*. Mech Dev 148, 3–10.

Martin AC, Kaschube M, Wieschaus EF (2009). Pulsed contractions of an actin-myosin network drive apical constriction. Nature 457, 495–499.

Martins GG, Summers RG, Morrill JB (1998). Cells are added to the archenteron during and following secondary invagination in the sea urchin *Lytechinus variegatus*. Dev Biol 198, 330–342.

Munro EM, Odell GM (2002). Polarized basolateral cell motility underlies invagination and convergent extension of the ascidian notochord. Development 129, 13–24.

Odell GM, Oster G, Alberch P, Burnside B (1981). The mechanical basis of morphogenesis. I. Epithelial folding and invagination. Dev Biol 85, 446–462.

Piston DW, Summers RG, Knobel SM, Morrill JB (1998). Characterization of Involution during sea urchin gastrulation using two-photon excited photorelease and confocal microscopy. Microsc Microanal 4, 404–414.

Ransick A, Davidson EH (1998). Late specification of Veg1 lineages to endodermal fate in the sea urchin embryo. Dev Biol 195, 38–48.

Rauzi M, Lenne PF, Lecuit T (2010). Planar polarized actomyosin contractile flows control epithelial junction remodelling. Nature 468, 1110–1114.

Schindelin J, Arganda-Carreras I, Frise E, Kaynig V, Longair M, Pietzsch T, Preibisch S, Rueden C, Saalfeld S, Schmid B, *et al.* (2012). Fiji: an open-source platform for biological-image analysis. Nat Methods 9, 676–682.

Schneider CA, Rasband WS, Eliceiri KW (2012). NIH Image to ImageJ: 25 years of image analysis. Nat Methods 9, 671–675.

Schoenwolf GC, Alvarez IS (1989). Roles of neuroepithelial cell rearrangement and division in shaping of the avian neural plate. Development 106, 427–439.

Shindo A, Inoue Y, Kinoshita M, Wallingford JB (2018). PCP-dependent transcellular regulation of actomyosin oscillation facilitates convergent extension of vertebrate tissue. Dev Biol 446, 159–167.

Simoes Sde M, Blankenship JT, Weitz O, Farrell DL, Tamada M, Fernandez-Gonzalez R, Zallen JA (2010). Rho-kinase directs Bazooka/Par-3 planar polarity during *Drosophila* axis elongation. Dev Cell 19, 377–388.

Simoes Sde M, Mainieri A, Zallen JA (2014). Rho GTPase and Shroom direct planar polarized actomyosin contractility during convergent extension. J Cell Biol 204, 575–589.

Umetsu D, Aigouy B, Aliee M, Sui L, Eaton S, Julicher F, Dahmann C (2014). Local increases in mechanical tension shape compartment boundaries by biasing cell intercalations. Curr Biol 24, 1798–1805.

Vanderleest TE, Smits CM, Xie Y, Jewett CE, Blankenship JT, Loerke D (2018). Vertex sliding drives intercalation by radial coupling of adhesion and actomyosin networks during *Drosophila* germband extension. Elife 7, e34586.

Walck-Shannon E, Hardin J (2014). Cell intercalation from top to bottom. Nat Rev Mol Cell Biol 15, 34–48.

Walck-Shannon E, Reiner D, Hardin J (2015). Polarized Rac-dependent protrusions drive epithelial intercalation in the embryonic epidermis of *C. elegans*. Development 142, 3549–3560.

Weliky M, Minsuk S, Keller R, Oster G (1991). Notochord morphogenesis in *Xenopus laevis*: simulation of cell behavior underlying tissue convergence and extension. Development 113, 1231–1244.

Weliky M, Oster G (1990). The mechanical basis of cell rearrangement. I. Epithelial morphogenesis during *Fundulus* epiboly. Development 109, 373–386.

Wessel GM, Wikramanayake A (1999). How to grow a gut: ontogeny of the endoderm in the sea urchin embryo. Bioessays 21, 459–471.

Williams M, Yen W, Lu X, Sutherland A (2014). Distinct apical and basolateral mechanisms drive planar cell polarity-dependent convergent extension of the mouse neural plate. Dev Cell 29, 34–46.

Williams-Masson EM, Heid PJ, Lavin CA, Hardin J (1998). The cellular mechanism of epithelial rearrangement during morphogenesis of the *Caenorhabditis elegans* dorsal hypodermis. Dev Biol 204, 263–276.

Wokosin DL, Centonze VE, White JG, Hird SN, Sepsenwol S, Malcolm GPA, Maker GT, Ferguson AI (1996). Multiple-photon excitation imaging with an all-solid-state laser. SPIE 2678, 38–49.